Acta Astronautica 240 (2026) 384–397

Contents lists available at ScienceDirect

Acta Astronautica

journal homepage: www.elsevier.com/locate/actaastro

Research paper

A model-based control framework for space debris management

Martina Rusconi *,[1], Camilla Colombo[2]

Politecnico di Milano, Department of Aerospace Science and Technology, Via la Masa 34, Milan, 20156, Italy

ARTICLE INFO

Keywords:
Space debris
Control
Evolutionary model
Mitigation policy
Sustainable space

ABSTRACT

The accelerating proliferation of space debris represents a serious and growing threat to the long-term sustainability of space operations. While modeling tools and mitigation guidelines have been developed over recent decades, the rapid expansion of commercial space activities has outpaced current regulatory mechanisms, which have struggled to keep pace with the rapidly evolving space mission environment. In response to this challenge, the GREEN SPECIES project, funded by the European Research Council, proposes an integrated, interdisciplinary framework for the robust control of the orbital environment. This work introduces a foundational element of the framework. A simplified one-dimensional statistical model of debris evolution is combined with a state-dependent linear feedback controller based on the differential Riccati approach. The model captures the dynamics of active satellites, inactive objects, and fragments across altitude shells, accounting for drag, launches, collisions, and disposal actions. The controller dynamically allocates mitigation actions such as post-mission disposal and active debris removal to steer the system towards a sustainability target defined by quantitative indices. This is achieved while minimizing a quadratic cost function and incorporating soft operational constraints, including the risk associated with removal operations and the cost of high-altitude activities. Results demonstrate the effectiveness of this approach in approximating desired environmental outcomes while optimizing resource use, offering practical insights for adaptive, cost-effective debris management. By linking control theory with debris evolution modeling, the GREEN SPECIES framework provides a novel policy-support tool for sustainable space governance.

1. Introduction

At the dawn of the space age, Earth's orbital environment was viewed as an infinite resource. Yet in under a century, rapid technological progress and reduced launch costs have led to a sharp rise in orbital traffic and with it, the growing problem of space debris. Concern about debris proliferation was first formalized in the 1970s, when Kessler and Cour-Palais warned of the potential for exponential debris growth and its associated risk of collision [1]. Without adequate intervention, this growth threatens the long-term sustainability of space operations. Since the late 20th century, various studies have aimed to understand and forecast debris dynamics using observational data and numerical models (e.g., [2–4]). Space agencies and research institutions such as the European Space Agency (ESA), the National Aeronautics and Space Administration (NASA), and the Italian National Research Council (CNR) have developed tools, such as DELTA [5], LEGEND [6], and SDM [7] to simulate the evolution of the orbital environment. These models support scientific investigations and sensitivity analyses into how different mitigation strategies such as Post-Mission Disposal (PMD), Active Debris Removal (ADR), and changes in launch traffic affect future projections of the space debris scenarios [8,9]. Based on those studies, in 2002, the Inter-Agency Space Debris Coordination Committee (IADC) issued guidelines promoting best practices for debris mitigation [10]. Yet, the rapid growth of the commercial space sector, particularly the deployment of large constellations and increased launch frequency, has outpaced current regulatory mechanisms. Recent studies in the annual Environment Report from ESA show that for different extrapolation scenarios of the current behavior in terms of space debris mitigation, the orbital environment becomes unstable, with collision rates increasing exponentially [11], underscoring the need for more adaptive policy tools. Like climate change, space debris represents a global environmental challenge. Climate science has long used Integrated Assessment Models (IAMs), such as DICE [12], to guide policies definition. A similar integration of modeling and decision-making is now emerging in space governance to face the need for policy mechanisms that are more responsive to a rapidly changing situation. The GREEN SPECIES project, funded by the European Research Council

* Corresponding author.
E-mail addresses: martina.rusconi@polimi.it (M. Rusconi), camilla.colombo@polimi.it (C. Colombo).
[1] PhD Student, Department of Aerospace Science and Technology.
[2] Professor, Department of Aerospace Science and Technology.

https://doi.org/10.1016/j.actaastro.2025.12.018
Received 30 September 2025; Received in revised form 28 November 2025; Accepted 8 December 2025
Available online 10 December 2025

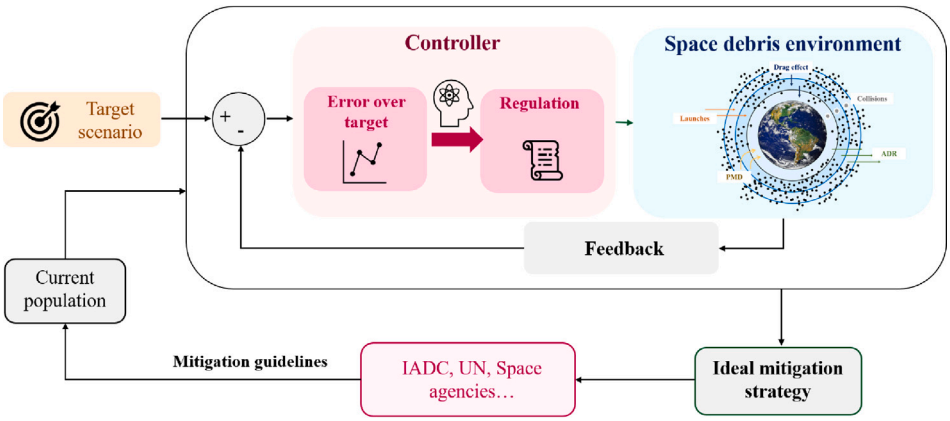

Fig. 1. GREEN SPECIES framework. A feedback controller acts on a predictive model to obtain ideal mitigation strategies in support to the definition of debris mitigation guidelines.

through a Consolidator Grant proposes an interdisciplinary framework for the robust control of space debris, with the goal of identifying optimal strategies ensuring long-term sustainability.

In this paper we adopt an adaptive feedback approach to manage the complex and evolving space debris environment across large spatial domains. A simplified framework of the work described in the paper is given in Fig. 1.

At the heart of the methodology lies the integration of a control mechanism with a statistical model of debris evolution. Unlike traditional models that rely on fixed-rate or trial-and-error mitigation strategies, this framework introduces a controller that dynamically adjusts actions (e.g., ADR) to meet defined space population targets..

A variety of debris modeling approaches has been developed in the literature. Early statistical representations include the Particle-In-a-Box (PIB) models such as the works by Farinella and Cordelli [13], Talent [2], Finkleman [14] and other systems like FADE [15], STAT [3], MISSD [16], MOCAT-SSEM [17] and, more recently, IMMEDIACY [18]. These approaches classify objects into groups with similar physical properties or occupying the same phase-space, and propagate the dynamics of the number of objects per category under dominant and simplified orbital effects, analyzing the impact of human activities without propagating individual objects. This approach, and specifically the source–sink MISSD model by Somma et al. [16], was selected as baseline for the development of an in-house source–sink model. In this work, however, the population is modeled as a continuous density field evolving under continuous orbital dynamics and external human influences. Continuum-based models treat the debris population as a continuous flow. First proposed by Heard in the 1970s [19], this approach was extended analytically by McInnes to describe density propagation in Low-Earth Orbit (LEO) under the effect of aerodynamic drag [20]. Continuum dynamics has then been used to analyze the evolution of the space debris environment in the SDPA model by Smirnov et al. [21], adopting a multi-phase approach to describe classes of objects evolving under simplified environmental forces and sources of fragmentation debris. The continuum approach to describe the evolution of a cloud of debris was further refined into the CiELO suite, which integrates the NASA breakup model [22] to define the initial distribution of fragments and applies the method of characteristics to analytically propagate the objects' density across orbital altitudes under aerodynamic drag [23]. Subsequent extensions have incorporated propagation in multiple dimensions through orbital elements and considering more realistic dynamics, including J_2 perturbations and solar radiation pressure (e.g. in the Starling suite [24,25]). More recently, continuum mechanics has been applied to model the overall LEO population in a one-dimensional space parametrized by orbital radius in [26], analyzing the cascade effect of fragmentations in [27] and the influence of launch traffic models [28]. These works led to the development of the COMETA tool [4], that combines probabilistic simulations of debris evolution with deterministic propagation of larger objects, under various force models, in-orbit breakups and mitigation actions. Similarly to previous works by Colombo et al. [26], Duran et al. [27] and Giudici et al. [4], the population of objects is modeled in this work as a continuous density field evolving under orbital dynamics and external human influences.

In recent years, active control has begun to emerge as a promising extension to debris modeling. Initial efforts such as CASCADE [29] and MISSD [16] used adaptive and proportional controllers to modulate ADR rates based on predicted debris trends. The previous work by Somma et al. [16] was one of the first applications of a control logic to automatically assign ADR operations to manage the evolution of the space environment. In his work Somma exploited proportional control based on the density evolution of objects in the model to allocate ADR rates per shell and object category. More advanced strategies, such as those implemented in MOCAT-SSEM [17], employ Model Predictive Control (MPC) to optimize mitigation and launch decisions across multiple object families. Nonetheless, the literature on feedback control for orbital debris remains limited, and this study contributes to that growing field. By exploring the interaction between active control and environmental dynamics, it aims to inform space policy makers and space users with results and considerations on ideal future mitigation approaches, and contribute to the design of cost-effective, adaptive strategies for maintaining sustainable space activity. The present work introduces a linear feedback controller within a one-dimensional, density-based model of debris propagation. The system is formulated in a quasi-linear fashion to allow application of well-established control techniques, moreover, its reduced dimensionality enables computational efficiency while retaining essential dynamics. Proportional feedback is employed as a first step due to its simplicity, robustness, and responsiveness to system evolution. The controller is based on a Riccati formulation and operates in altitude shells, enabling optimal mitigation under environmental and operational constraints.

The proposed methodology sets as an alternative active control of mitigation measures for space environment evolution, becoming part of the very restricted literature on the topic. The model development is still ongoing and under improvement. Being aware of the current limitations, the novel methodology is used in this paper to show the versatility and potential usage of the GREEN SPECIES framework, with no claims on realism of results. The paper is organized as follows: in Section 2 the environmental model is described in all its parts, the controller is detailed in Section 3; then, an application of the overall system and discussion of the results are in Section 4 with final conclusions drawn in Section 5.

2. The model

A statistical model of limited dimensionality is advantageous from a control systems perspective. Applying modern robust control techniques to highly non-linear, multidimensional systems would be computationally prohibitive and often infeasible.

In this context, a novel integration of a density-based approach with active control is employed to represent the spatial evolution of the distribution of objects. The population of Earth-orbiting objects is modeled as a continuous flow evolving in a one-dimensional space, influenced by environmental forces, sources, and sinks. The LEO region, spanning altitudes between 200 km and 2000 km, is discretized into spherical shells of constant thickness equal to 50 km in this work. This value is the same as in [16] and sets as a compromise between computational resources and finer domain discretization. The larger the dimensionality of the problem the more resource consuming the controller task. The only spatial dimension considered is the orbital radius, used to identify each bin. From a given reference population of orbiting objects, the spatial density in each shell is derived based on the orbital parameters of the same: semi-major axis (a), eccentricity (e), and orbital radius (r), using the methodology outlined by Kessler [30] in Eq. (1).

$$n_j(r) = \frac{1}{4\pi^2 r a^2 \sqrt{e^2 - (\frac{r}{a} - 1)^2}} \qquad n(r) = \Sigma_{j=1}^{N} n_j(r) \tag{1}$$

Each object's contribution to a shell is weighted by the time it spends in an infinitesimal volume around the central radius of that shell. The total density at a given radius is then obtained by summing all contributions of the N objects in the initial population. This formulation sacrifices information about the precise orbital shape, effectively treating all orbits as circular.

The evolution of the initial density profile is governed by the conservation of the total number of objects in time and space, enforced through the integral form of the conservation law, typically used in fluid dynamics [31], the continuity Equation (2), where the density (n) evolution in time (t) is given under environmental dynamics (v_r is the radial velocity in the shell) and space activities in terms of density rates for sources and sinks ($\dot{n}^+$ and $\dot{n}^-$), within each volume (V).

$$\int_{V_i} \frac{\partial n}{\partial t} dV = -\int_{V_i} \nabla(n \cdot v_r) dV + \int_{V_i} (\dot{n}^+ - \dot{n}^-) dV \tag{2}$$

Assuming the density remains constant within each bin, the finite volume method is applied (similarly to [32,33]). The divergence theorem [34] is used to rewrite the continuity Equation (2) in the form of Eq. (3), where S denotes the shell boundary surface.

$$\frac{dn}{dt} = \frac{1}{V}\left[-\int_S (v_r n) dS + \int_V \dot{n}^+ - \int_V \dot{n}^-\right] \tag{3}$$

In the present model, Eq. (3) is propagated in time in the discretized domain shown in Fig. 2 under major environmental perturbations and sources and sinks.

The initial population is categorized into three species: intact active objects, intact inactive objects, and small debris. Using data sources such as the DISCOS database [35], payloads and rocket bodies are included under the first two categories. Each object type is assigned a typical operational lifetime, which can be customized for each application. Objects in orbit for less than this period are considered active and part of the first species; those exceeding 8 years (for payloads in this work and similarly to [11,16,36]) or 0.001 years (for rocket bodies with an operational lifetime approximately null) are classified as inactive and part of the second species. Large debris with cross-sectional area larger than 1 m^2 are also included in the inactive category, while smaller debris fall into the debris group. Currently, the model considers only three species to maintain tractability. For each, the first term in Eq. (2) accounts for the stretching of shell volumes due to environmental effects, which is translated in terms of flow passing through a fixed volume in the form of Eq. (3).

In LEO, atmospheric drag is the dominant perturbation over long time scales; shorter-term perturbations such as the J_2 effect are neglected due to the long-term nature of the analysis performed and the radial dimensionality of the problem selected. The evolution of the shell radius r (i.e. radial velocity v_r) is computed using the King-Hele drag model [37] in Eq. (4), where μ and r_E are Earth's gravitational parameter and radius respectively; $\frac{A}{m}$ is the area over mass ratio associated to each species, which is taken as the average value of the initial population groups (as in [16,36]), and C_D is the drag coefficient set to 2.1 under flat plates assumption. Atmospheric density is modeled as a sum of exponentials representing n_p partial atmospheres, each with reference density ($\hat{\rho}_p$) and scale height ($\hat{H}_p$), as proposed in [38].

$$v_r = -\sqrt{\mu r}\frac{A}{m} C_D \sum_{p=1}^{n_p} \hat{\rho}_p \exp(-\frac{r - r_E}{\hat{H}_p}) \tag{4}$$

As a first approach no time-varying solar flux is included, but it could be easily implemented given the time-dependency of the system. The drag effect is applied only to inactive objects and fragments, as active objects are assumed to maintain a fixed orbit during their operative life and perform manoeuvres to counteract environmental disturbances.

The sources and sinks modeled include: launch traffic, PMD, ADR, and collisions between active objects and fragments, between two intact inactive objects, and between intact objects and fragments. It is assumed that active satellites can avoid large debris but remain vulnerable to small particles, while inactive objects lack manoeuvring capability and may collide with one another or with smaller fragments. Collisions between fragments are excluded due to their small cross-sectional areas and resulting low collision probabilities. Future versions of the model will incorporate collision avoidance reliability for active objects. The full dynamical system is summarized in Eq. (5), defined for each of the N shells identified between lower and upper radii, r_{lower} and r_{upper}, and the three species: active objects (ao), inactive objects (io) and fragments (fr). For each species the terms that affect their dynamics in Eq. (5) are explicitly addressed in the following.

Environmental effects influence inactive objects and fragments, while human activity affects intact objects: launches generate active satellites; disposal and ADR reduce the inactive population. In-orbit collisions interlink all three species.

$$\begin{cases} \frac{dn_{ao_i}}{dt} = \frac{1}{V}\left[+\frac{N_{i_L}}{1year} - \int_{V_{i_L}} \frac{\dot{n}_{i_L}(t_L)}{1year} - \dot{\eta}_{ao-f}\right] \\ \frac{dn_{io_i}}{dt} = \frac{1}{V}\left[-\left(4\pi n_{io_{i+1}} v_{r_{i+1}} r^2_{i_{upper}} - 4\pi n_{io_i} v_{r_i} r^2_{i_{lower}}\right) + \right. \\ \qquad \left. + (1-\beta)\int_{V_{i_L}} \frac{\dot{n}_{i_L}(t_L)}{1year} - \alpha\frac{N_{i_{ADR}}}{1year} - 2\dot{\eta}_{io-io} - \dot{\eta}_{io-f}\right] \\ \frac{dn_{fr_i}}{dt} = \frac{1}{V}\left[-\left(4\pi n_{fr_{i+1}} v_{r_{i+1}} r^2_{i_{upper}} - 4\pi n_{fr_i} v_{r_i} r^2_{i_{lower}}\right) + \right. \\ \qquad \left. - \dot{\eta}_{ao-fr} - \dot{\eta}_{io-fr} + \dot{\eta}_{ao-fr} N_{c_{ao-fr}} + \dot{\eta}_{io-fr} N_{c_{io-fr}} + \dot{\eta}_{io-io} N_{c_{io-io}}\right] \\ \vdots \quad \text{for} \quad i = 1, \dots, N_s \end{cases} \tag{5}$$

Launch traffic is modeled as the repetition of historical data from a fixed number of years preceding the simulation start date, consistent with methods in [4,39]. Yearly launch rates (in Eq. (5): $N_{i_L}/1year$) are translated into density deposition terms for the active object population.

PMD is assumed to be necessary for orbital shells situated above a certain altitude, defined by a re-entry constraint, typically 25 years to re-entry [10]. Objects below this altitude threshold are considered to re-enter below the atmosphere limit set at 200 km altitude within

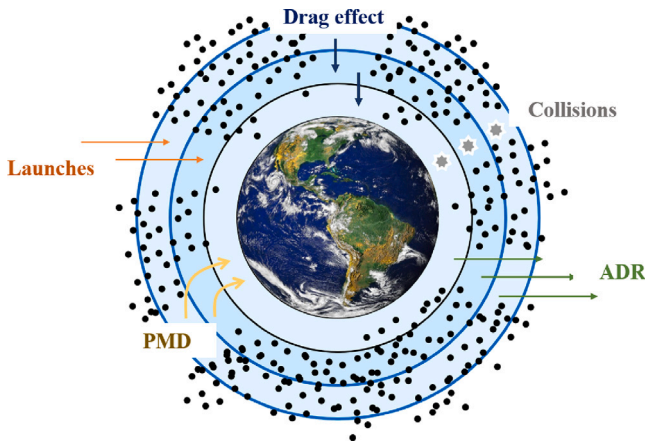

Fig. 2. Visual representation of the predictive model and the main contributions modeled.

an acceptable time frame, and thus do not require PMD at End-of-Life (EOL). In the case of the 25-year re-entry criterion, disposal actions are undertaken only for objects in shells above 630 km. This requirement is obtained solving the relation in Eq. (6) proposed by King-Hele, that defines the time that an object takes to move from an orbital radius r_{PMD} to the re-entry limit r_0 under the atmospheric drag model in [37].

$$t_{PMD} = \frac{(1-\exp(-\frac{1}{H_{r_{PMD}}})(r_{PMD}-r_0))H_{r_{PMD}}\sqrt{\frac{r_{PMD}^3}{\mu}}}{\rho_{r_{PMD}}\frac{A}{m}C_D r_{PMD}^2} \tag{6}$$

For shells below this threshold, the drag model described in [37] ensures that re-entry occurs within the prescribed time frame. At time t, based on the launch traffic considered, the number of active objects reaching EOL in the considered shell is computed. The objects available for disposal (in Eq. (5)): $\int_{V_{t_L}} \dot{n}_{i_L}(t_L)/1year$) were launched at $t_L = t - t_{L->PMD}$ with $t_{L->PMD}$ the operational time of the species between launch and the beginning of the disposal phase. These are reclassified as inactive and a fraction β of them is immediately transferred to the first shell below the re-entry altitude. So, a β percentage of them is assumed to perform successful disposal.

Due to the lack of reliable data on the evolution of ADR technology, removals are modeled as a fixed annual removal rate per shell: $\alpha N_{i_{ADR}}/1year$ in Equation (5), with α representing the fraction of a predefined maximum of removals per volume $N_{i_{ADR}}$.

Following Kessler's theory [1] and more recent findings, on-orbit collisions are the primary driver of debris proliferation. The model incorporates collisions using the approach from [16], which calculates the number of fragments generated as a product of impact rates ($\dot{\eta}$ in Eq. (5)) and species-specific collision outcomes. Only three types of collisions are modeled: active objects with fragments, two intact inactive objects, and intact objects with fragments. As strong assumption all debris are assumed to remain in the shell where the collision occurred and only objects down to 10 cm-range are considered in the analysis. Collision rate $\dot{\eta}$ is defined using the kinetic theory of gases, following Eq. (7) from [30]. The average cross-sectional areas σ_{ao} and σ_{io} of the larger objects in the collision is fixed and derived as the average of the initial population categories. Fragments' cross-sectional area is assumed negligible with respect to the intact objects ones. v_{c_i} is the relative impact velocity between the colliding objects in the shell, adopting the approach in [2,16], it is assumed equal to $\sqrt{2}v_{r_i}$. Collisions are all treated as catastrophic and the number of generated fragments for each case ($N_{c_{ao-fr}}$, $N_{c_{io-io}}$ and $N_{c_{io-fr}}$ in Eq. (5)) is calculated using the NASA Standard Breakup Model (SBM) relations [22].

$$\begin{aligned}
\dot{\eta}_{ao-fr} &= \sigma_{ao} v_{c_i} n_{ao_i} n_{fr_i} V_i \\
\dot{\eta}_{io-io} &= \frac{1}{2}\sigma_{io} v_{c_i} n_{io_i}(n_{io_i} V_i - 1) \\
\dot{\eta}_{io-fr} &= \sigma_{io} v_{c_i} n_{io_i} n_{fr_i} V_i
\end{aligned} \tag{7}$$

Future developments will address better modeling of fragments redistribution across shells and incorporation of explosions, either as fixed yearly events or as probability-based occurrences per object class [36]. While the current work benefits from the use of a simplified, low-dimensional model that facilitates integration with control systems, future work will interface the developed strategies with COMETA [4], a more complex and realistic environmental model of the space object population. This will allow for a more accurate assessment of the controller's performance in operationally relevant scenarios.

3. The controller

The model described in Section 2 predicts the evolution of the space environment in terms of the distribution of orbiting objects. The increasing attention on space debris has raised critical concerns on how to limit their proliferation. In response, recent missions are designed incorporating EOL disposal strategies to prevent the accumulation of inactive satellites in the most crowded orbital regions. Additionally, technologies for ADR are being developed to reduce existing debris. Historically, studies have focused on identifying mitigation actions. However, the focus has now shifted to determining how to apply these actions effectively and cost-efficiently to maximize adoption and environmental benefit. To address this, we use the simplified model of Section 2 with a dynamics-informed control approach, exploiting the system's expected behavior, to allocate mitigation resources efficiently. The logic described in this Section is general and adaptable to various application cases, an example of which is in Section 4, where each of the terms generally discussed in the following takes a specific formulation.

This study employs the State-Dependent Differential Riccati (SDDRE) control in its general form [40–42]. This optimal control technique relies on the well-established linear control theory to minimize a performance function through a feedback control loop. To interface with the controller the model is expressed in a state-space representation (see Eqs. (8) and (9)), where the state vector $\mathbf{x}$ contains densities of active and inactive objects and fragments per orbital shell, following the system in Eq. (5).

$$\dot{\mathbf{x}} = \mathbf{F}(t,\mathbf{x})\mathbf{x} + \mathbf{G}(t,\mathbf{x},\mathbf{u})\mathbf{u} + \mathbf{C}(t,\mathbf{x}) \tag{8}$$

$$\mathbf{y} = \mathbf{L}(t,\mathbf{x})\mathbf{x} \tag{9}$$

where:

$$\dot{\mathbf{x}} = \begin{bmatrix} \mathbf{x}_{ao}^{\cdot} \\ \mathbf{x}_{io}^{\cdot} \\ \mathbf{x}_{fr}^{\cdot} \end{bmatrix}$$

$$\mathbf{F} = [\mathbf{F}_d(t) + \mathbf{F}_c(t,\mathbf{x})]$$

$$\mathbf{F}_d = \begin{bmatrix} \mathbf{0} & \mathbf{0} & \mathbf{0} \\ \mathbf{0} & \mathbf{F}_{\mathbf{d}_{\mathbf{N_s}}} & \mathbf{0} \\ \mathbf{0} & \mathbf{0} & \mathbf{F}_{\mathbf{d}_{\mathbf{N_s}}} \end{bmatrix} \tag{10}$$

$$\mathbf{F}_{d_{N_s}} = \begin{bmatrix} F_{d_{1,1}} & F_{d_{1,2}} & 0 & \dots & 0 \\ 0 & \ddots & \ddots & & \\ \vdots & & F_{d_{i,i}} & F_{d_{i,i+1}} & \\ & & & \ddots & \ddots \\ 0 & & & & F_{d_{N,N}} \end{bmatrix}$$

$$F_{d_{i,i}} = \frac{1}{V_i}(4\pi v_{r_i} r_{i_{lower}}^2)$$

$$F_{d_{i,i+1}} = -\frac{1}{V_i}(4\pi v_{r_{i+1}} r_{i_{upper}}^2)$$

$$\mathbf{F}_c = \begin{bmatrix} \mathbf{F}^{-}_{\mathbf{c}_{ao-fr}} & \mathbf{0} & \mathbf{0} \\ \mathbf{0} & \mathbf{F}^{-}_{\mathbf{c}_{io-io}} + \mathbf{F}^{-}_{\mathbf{c}_{io-fr}} & \mathbf{0} \\ \mathbf{F}^{\pm}_{\mathbf{c}_{ao-fr}} & \mathbf{F}^{+}_{\mathbf{c}_{io-io}} + \mathbf{F}^{\pm}_{\mathbf{c}_{io-fr}} & \mathbf{0} \end{bmatrix} \tag{11}$$

$$\mathbf{F}^{\pm}_{\mathbf{c}_{s1-s2}} = \begin{bmatrix} F^{\pm}_{s1-s2_{1,1}} & 0 & \dots & 0 \\ 0 & F^{\pm}_{s1-s2_{i,i}} & 0 & \dots \\ \vdots & & \ddots & \end{bmatrix}$$

$$F^{-}_{ao-fr_{i,i}} = -\sigma_{ao} v_{r_i} x_{fr_i}$$

$$F^{-}_{io-io_{i,i}} + F^{-}_{io-fr_{i,i}} = -\frac{1}{V_i} v_{r_i} \sigma_{io} (x_{io_i} V_i - 1) - \sigma_{io} v_{r_i} x_{fr_i}$$

$$F^{\pm}_{ao-fr_{i,i}} = (N_{c_{ao-f}} - 1) \sigma_{ao} v_{r_i} x_{fr_i}$$

$$F^{+}_{io-io_{i,i}} + F^{\pm}_{io-fr_{i,i}} = \frac{1}{V_i} v_{r_i} \sigma_{io} (x_{io_i} V_i - 1) N_{c_{io-io}} + (N_{c_{io-fr}} - 1) \sigma_{io} v_{r_i} x_{io_i}$$

The state matrix $\mathbf{F}$ comprises drag ($\mathbf{F}_d$), that is time-varying and defined as in Eq. (10). Following the finite volume approach $\mathbf{F}_d$ identifies the density variation caused by the objects entering ($\mathbf{F}_{d_{i,i}}$) and exiting ($\mathbf{F}_{d_{i,i+1}}$) a shell i due to drag effect. The collision term ($\mathbf{F}_c$) in $\mathbf{F}$ is also state-dependent as defined in Eq. (11). All the collision contributions described in Section 2 are explicitly reported as the product between the collision rates, taken from Eq. (7) in terms of state $\mathbf{x}$, and the density variation. The latter is the number of objects removed (identified by the − contributions in Eq. (11)) and fragments generated (identified by the + contributions in Eq. (11)) within a volume shell.

The control matrix $\mathbf{G}$ maps the control actions on the environment as density rates, while the vector $\mathbf{C}$ accounts for additional disturbances. State, control and time dependencies in Eq. (8) allow incorporating control constraints and limitations through $\mathbf{G}$. For the application to space debris mitigation the control actions defining $\mathbf{u}$ may include launch rates or PMD and ADR rates and compliance. The definition of the control inputs shapes the structure of $\mathbf{G}$ and $\mathbf{C}$, both potentially time- and state- or control-dependent, as will be presented more in details in the application of Section 4.

Any non-linear system can be factorized into a linear form, enabling the matrices to be state- or control-dependent, keeping the non-linearity and non-affinity of the system. The parametrization in Eq. (8) is not the unique option available to linearize the system through factorization, but it is chosen to link object types via collisions, ensuring system controllability. The type of factorization adopted impacts control performance, as proved in the work on methods for optimal factorization in [43], but this is not treated here.

The output vector $\mathbf{y}$ (Eq. (9)) represents the performance metric that one wants to manipulate though the controller, it is factorized with the target matrix $\mathbf{L}$ and its formulation is application-dependent based on the choice of the output $\mathbf{y}$ (see an example in Section 4).

An optimal control problem is formulated to minimize a typical quadratic cost function with a quadratic term at the terminal state and a quadratic integral term in state and control [44]. The performance value defined in Eq. (12) accounts for the integral of the output error: $\mathbf{e} = \mathbf{y} - \mathbf{y}_t$ with respect to a reference profile ($\mathbf{y}_t$) and of the control effort throughout the simulation, both are subject to positive-definite weighting matrices $\mathbf{A}$ and $\mathbf{B}$. Finally, a terminal penalty on the error of the manipulated output weighted on the positive-definite $\mathbf{S}_f$ matrix is added to the cost function J.

$$J = \frac{1}{2} \mathbf{e}^T \mathbf{S}_f(t, \mathbf{x}) \mathbf{e} + \frac{1}{2} \int_{t_0}^{t_f} \left(\mathbf{e}^T \mathbf{A}(t, \mathbf{x}) \mathbf{e} + \mathbf{u}^T \mathbf{B}(t, \mathbf{x}) \mathbf{u} \right) dt \tag{12}$$

The weighting matrices are used to scale the relative importance of each term contributing to the performance function in Eq. (12), and consequently are affecting the control logic behavior: to solve the optimal minimization problem the controller will act on decreasing the heaviest contribution to the performance function, optimizing efficiency of the actions. Moreover, the weighting matrices can be used to translate external soft constraints (i.e. not strictly enforced, but added as large penalty contributions to the performance function so that their violation would cause an unacceptable cost increase) and known desirable behaviors into penalties in the cost, e.g. enabling prioritization of specific orbital regions assigning larger penalties to those regions we care most about controlling. Examples of this are given in Section 4.

The control logic in time is derived using standard optimal control methods [44] to obtain a time-profile of the $\mathbf{u}$ allocation for minimization of J, which must be accurately set to identify a balance between performance in reaching the target and control effort used. The optimality conditions in the form of Euler–Lagrange Equations (13) are enforced, where the Hamiltonian is defined as $H = 1/2 \mathbf{e}^T \mathbf{A} \mathbf{e} + \mathbf{u}^T \mathbf{B} \mathbf{u} + \lambda^T (\mathbf{F}\mathbf{x} + \mathbf{G}\mathbf{u} + \mathbf{C})$, with λ the co-state vector.

$$\begin{aligned} &\frac{\partial H}{\partial \mathbf{u}} = 0 \\ &\frac{\partial H}{\partial \mathbf{x}} = -\dot{\lambda} \\ &\frac{\partial (\frac{1}{2} \mathbf{e}^T \mathbf{S}_f(t, \mathbf{x}) \mathbf{e})_f}{\partial \mathbf{x}(t_f)} = \lambda_f^T \end{aligned} \tag{13}$$

Exploiting the linearity of the system the co-state can be assumed to take the form $\lambda = \mathbf{S}\mathbf{x} + \mathbf{W} + \mathbf{D}$ (sweep-method in [44]). Then, applying the calculus of variations to the first optimality condition yields the control law in Eq. (14), where $\mathbf{W}$ and $\mathbf{D}$ have been added to the standard proportional gain expression of linear feedback controllers to track a reference trajectory $\mathbf{y}_t$ and reject state- and control-independent disturbances in $\mathbf{C}$, respectively.

$$\mathbf{u} = -\mathbf{B}^{-1} \mathbf{G}^T (\mathbf{S}\mathbf{x} + \mathbf{W} + \mathbf{D}) \tag{14}$$

From the second condition for optimality in Eq. (13), state- and time-dependent differential relations of the gain matrices are obtained. With them, enforcing the final conditions on λ through the third relation of Eq. (13), the time profiles of the gain matrices in Eq. (14) are solved with backward propagation. Specifically, $\mathbf{S}$ solves the state-dependent Riccati Equation (15) with the final condition on $\mathbf{S}_f$ defined, extending the standard Riccati approach used in [45]. $\mathbf{W}$ and $\mathbf{D}$ are obtained by solving backward the differential Eqs. (16) and (17) subject to the corresponding final conditions on $\mathbf{W}_f$ and $\mathbf{D}_f$ [40,44,46]. The explicit dependencies of each term from time, state and control have been omitted for clarity of the text.

$$\begin{aligned} \dot{\mathbf{S}} = &-\mathbf{S}\mathbf{F} + \mathbf{S}\mathbf{G}\mathbf{B}^{-1}\mathbf{G}^T\mathbf{S} - \mathbf{L}^T\mathbf{A}\mathbf{L} - \mathbf{F}^T\mathbf{S} - \left(\frac{\partial \mathbf{F}}{\partial \mathbf{x}}\mathbf{x}\right)^T \mathbf{S} - \left(\frac{\partial \mathbf{L}}{\partial \mathbf{x}}\mathbf{x}\right)^T \mathbf{A}\mathbf{L} + \\ &- \frac{1}{2}\left(\frac{\partial \mathbf{A}}{\partial \mathbf{x}}\mathbf{L}\mathbf{x}\right)^T \mathbf{L} + \frac{1}{2}\left(\frac{\partial \mathbf{A}}{\partial \mathbf{x}}\mathbf{y}_T\right)^T \mathbf{L} - \left(\frac{\partial \mathbf{G}}{\partial \mathbf{x}}\mathbf{u}\right)^T \mathbf{S} + \\ &+ \frac{1}{2}\left(\frac{\partial \mathbf{B}}{\partial \mathbf{x}}\mathbf{u}\right)^T \mathbf{B}^{-1}\mathbf{G}^T\mathbf{S} - \left(\frac{\partial \mathbf{C}}{\partial \mathbf{x}}\right)^T \mathbf{S} \\ \mathbf{S}f = &\ \mathbf{L}_f^T \mathbf{S}_f \mathbf{L}_f + \left(\frac{\partial \mathbf{L}}{\partial \mathbf{x}}\mathbf{x}\right)_f^T \mathbf{S}_f \mathbf{L}_f \end{aligned} \tag{15}$$

$$\begin{aligned} \dot{\mathbf{W}} = &\ \mathbf{S}\mathbf{G}\mathbf{B}^{-1}\mathbf{G}^T\mathbf{W} - \mathbf{F}^T\mathbf{W} + \mathbf{L}^T\mathbf{A}\mathbf{y}_t - \left(\frac{\partial \mathbf{F}}{\partial \mathbf{x}}\mathbf{x}\right)^T \mathbf{W} + \left(\frac{\partial \mathbf{L}}{\partial \mathbf{x}}\mathbf{x}\right)^T \mathbf{A}\mathbf{y}_t + \\ &- \frac{1}{2}\left(\frac{\partial \mathbf{A}}{\partial \mathbf{x}}\mathbf{y}_t\right)^T \mathbf{y}_t + \frac{1}{2}\left(\frac{\partial \mathbf{A}}{\partial \mathbf{x}}\mathbf{L}\mathbf{x}\right)^T \mathbf{y}_t - \left(\frac{\partial \mathbf{G}}{\partial \mathbf{x}}\mathbf{u}\right)^T \mathbf{W} + \\ &+ \frac{1}{2}\left(\frac{\partial \mathbf{B}}{\partial \mathbf{x}}\mathbf{u}\right)^T \mathbf{B}^{-1}\mathbf{G}^T\mathbf{W} - \left(\frac{\partial \mathbf{C}}{\partial \mathbf{x}}\right)^T \mathbf{W} \\ \mathbf{W}_f = &-\mathbf{L}_f^T \mathbf{S}_f \mathbf{y}_{t_f} - \left(\frac{\partial \mathbf{L}}{\partial \mathbf{x}}\mathbf{x}\right)_f^T \mathbf{S}_f \mathbf{y}_{t_f} \end{aligned} \tag{16}$$

$$\begin{aligned} \dot{\mathbf{D}} = &\ \mathbf{S}\mathbf{G}\mathbf{B}^{-1}\mathbf{G}^T\mathbf{D} - \mathbf{F}^T\mathbf{D} - \mathbf{S}\mathbf{C} - \left(\frac{\partial \mathbf{F}}{\partial \mathbf{x}}\mathbf{x}\right)^T \mathbf{D} - \left(\frac{\partial \mathbf{G}}{\partial \mathbf{x}}\mathbf{u}\right)^T \mathbf{D} + \\ &+ \frac{1}{2}\left(\frac{\partial \mathbf{B}}{\partial \mathbf{x}}\mathbf{u}\right)^T \mathbf{B}^{-1}\mathbf{G}^T\mathbf{D} - \left(\frac{\partial \mathbf{C}}{\partial \mathbf{x}}\right)^T \mathbf{D} \\ \mathbf{D}_f = &\ \mathbf{0} \end{aligned} \tag{17}$$

A numerical approach is implemented for the propagations. However, solving Eqs. (15)–(17) backward requires future state information, which is not known a priori. Several methods address this, including

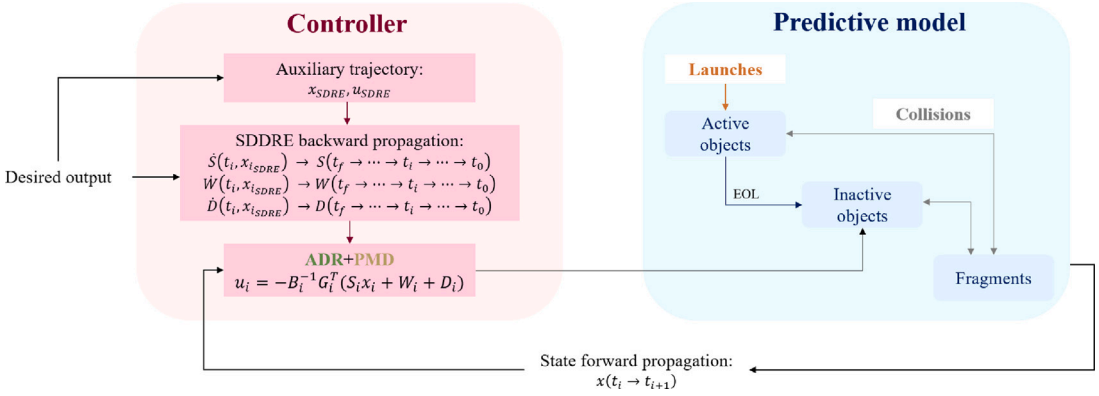

Fig. 3. Visual representation of the feedback control logic derivation and link with the predictive model.

forward integration with frozen coefficients [47], backward integration [42,46], sequential Riccati solutions [47], state transition matrix techniques [40], and Lyapunov-based approaches [42,46]. We adopt a sub-optimal State-Dependent Riccati Equation (SDRE) method to obtain an auxiliary trajectory for backward integration, using the algebraic approximation of Eqs. (15)–(17) dropping the state derivative terms (see Eqs. (18)–(20)) [40,42]. These SDREs are solved online using the Schur method [48].

$$\mathbf{SF} - \mathbf{S}_{SDRE}\mathbf{G}\mathbf{B}^{-1}\mathbf{G}^T\mathbf{S}_{SDRE} + \mathbf{L}^T\mathbf{A}\mathbf{L} + \mathbf{F}^T\mathbf{S}_{SDRE} = \mathbf{0} \tag{18}$$

$$\mathbf{S}_{SDRE}\mathbf{G}\mathbf{B}^{-1}\mathbf{G}^T\mathbf{W}_{SDRE} - \mathbf{F}^T\mathbf{W}_{SDRE} + \mathbf{L}^T\mathbf{A}\mathbf{y}_t = \mathbf{0} \tag{19}$$

$$\mathbf{S}_{SDRE}\mathbf{G}\mathbf{B}^{-1}\mathbf{G}^T\mathbf{D}_{SDRE} - \mathbf{F}^T\mathbf{D}_{SDRE} - \mathbf{S}_{SDRE}\mathbf{C} = \mathbf{0} \tag{20}$$

The overall procedure is summarized in Fig. 3: the controlled simulation is obtained by first solving for an auxiliary state profile numerically integrating in time the dynamics Equation (8) and the algebraic Eqs. (18), (19) and (20) to define the control logic in Eq. (14); then the auxiliary state trajectory is used to guide the backward integration of the gain matrices in Eqs. (15), (16) and (17) obtaining the time evolutions of the same that optimize the cost function acting on the system through Eq. (14). Finally, the controlled evolution of the model is retrieved forward propagating the state and output in Eqs. (8) and (9) under optimal SDDRE control, discretizing the process to preserve time-step control data.

The approach allows versatility of the control action that at each step adapts to the changing environment in feedback, providing insights on the most-suitable long-term mitigation plan to adopt based on future predictions.

The SDDRE method is versatile, adaptable to any non-linear and non-affine system that can be factorized. Different metrics, target scenarios, and dynamic models can be integrated into the framework, enabling automated and optimal control allocation. Though more computationally demanding than simpler control designs, its offline nature in the GREEN SPECIES framework makes this trade-off acceptable.

4. Application

An application of the framework described in Sections 2 and 3 is provided. In this example, a non-linear performance metric is adopted, and control is applied to the state-space model in Eqs. (8) and (9) to determine optimal allocations for ADR and PMD (see the case in Fig. 3), while incorporating practical constraints and preferences on both strategy and performance. A reference population, provided by the authors of [49], and set with a reference epoch of 2022, defines the initial orbital object density. The launch traffic term in Eq. (5) reflects a repetition of launch activity over the five years preceding the reference epoch and illustrated in Fig. 4. The control inputs in this application are the percentage of objects removed via ADR, denoted α in Eq. (5), and the percentage of end-of-life objects successfully disposed via PMD, denoted β in Eq. (5). The method in Section 3 is general and adaptable to other input combinations, provided the control matrices are updated accordingly. Control is applied only to orbital shells above 630 km, a threshold chosen because objects below this altitude are modeled to re-enter naturally within 25 years under King-Hele dynamics, that for this analysis is considered the threshold under which objects accumulation is accepted (future work will consider control application also at lower altitudes with a more thorough investigation of the increased launch traffic accumulation in that region). Above this threshold, the controller adjusts the PMD percentage β and the ADR percentage α over time. The number of controlled shells is denoted by j, so $\mathbf{u}$ acts from shell $N_s - j$ to shell N_s. The ADR maximum rate ($N_{i_{ADR}}$ in Eq. (5)) is set at a constant 5 removals per year in the whole domain, and both PMD and ADR percentages are saturated at 99% and 100%, respectively. As introduced in Section 3, the control logic is general and the choice of the target metric that is used to identify the final scenario may change, it could be the mere distribution of objects in the environment or it may be a more elaborated metric used to evaluate the health of the environment (e.g. [50,51]). The selected performance metric for this application is a shell-based index function defined in Eq. (21) for a shell i, and its initial distribution is shown in Fig. 5, along with the initial absolute error $\mathbf{e}$ of Eq. (12) and the initial share of the index in each shell of the domain (that will be used for the weighting matrices definitions).

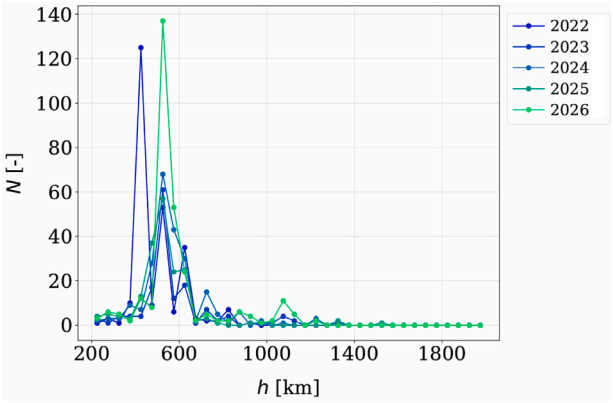

Fig. 4. 5 years cycle of number of launched objects per shell, which is repeated during the simulations.

$$y_i = \frac{\dot{\eta}_{ao-fr}}{\bar{\dot{\eta}}} \frac{N_{c_{ao-fr}}}{\bar{N}} \frac{t_{res_i}}{\bar{t}} + \frac{\dot{\eta}_{io-fr}}{\bar{\dot{\eta}}} \frac{N_{c_{io-fr}}}{\bar{N}} \frac{t_{res_i}}{\bar{t}} + \frac{\dot{\eta}_{io-io}}{\bar{\dot{\eta}}} \frac{N_{c_{io-io}}}{\bar{N}} \frac{t_{res_i}}{\bar{t}} \tag{21}$$

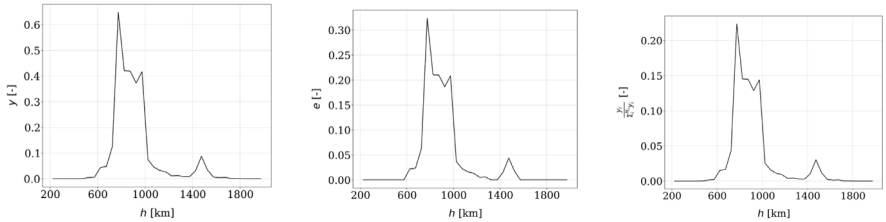

(a) Initial value of the index in Equation (21) in each shell of the domain.

(b) Initial distribution of the index absolute error on the target profile.

(c) Initial index share in each shell of the environment as the relative value of each bin on the sum of all the values in the domain.

Fig. 5. Initial distribution of the index in Eq. (21) (a). Initial absolute error of the index with respect to the target profile (the **e** parameter in Eq. (12)) (b). Initial index share in each shell of the environment (c).

The index is inspired from the Criticality of Spacecraft Index in [50]. The index has been slightly modified from [50] and in Eq. (21) it accounts for the contribution of all the collisions considered in the model: inactive objects-fragment, two inactive objects and active objects-fragment. For each term the product in Eq. (21) is computed between the collision rate $\dot{\eta}$ as defined in Eq. (7), the number of fragments from catastrophic collisions N_{c_j} generated from the NASA SBM relations [22], as in the model of Section 2, and the residency time t_{res} of the generated fragments. The latter is computed considering the time required for natural re-entry under the drag effect modeled with King-Hele approach in [37] from each shell of the environment and it is saturated at 100 years. Each contribution to the index is scaled by the reference values $\bar{\eta} = 5 \times 10^{-10}$, $\bar{N} = 1 \times 10^3$ and $\bar{t} = 100\ y$ to make it dimensionless. The control goal of the 100 years of simulation is to halve the index in all shells where it exceeds a threshold of 1×10^{-2}. Since the index is non-linear in the state, it is factorized in the form of Eq. (9) with the matrix in Eq. (22) to fit within the control framework.

$$\mathbf{L} = \begin{bmatrix} \frac{\sigma_{ao} v_{c_i} n_{fr_i} V_i}{\bar{\eta}} \frac{N_{c_{ao-fr}}}{\bar{N}} \frac{t_{res_i}}{\bar{t}} & \frac{\frac{1}{2}\sigma_{io} v_{c_i} (n_{io_i} V_i - 1)}{\bar{\eta}} \frac{N_{c_{io-io}}}{\bar{N}} \frac{t_{res_i}}{\bar{t}} & \\ 0 & \ddots & \ddots \\ & \frac{\sigma_{io} v_{c_i} n_{io_i} V_i}{\bar{\eta}} \frac{N_{c_{io-fr}}}{\bar{N}} \frac{t_{res_i}}{\bar{t}} & 0 \\ & \ddots & \end{bmatrix} \tag{22}$$

The environmental dynamics, including atmospheric drag and in-orbit collisions, are modeled as specified in Eq. (5). Given the choice of control inputs, the corresponding matrices **G** and **C** are defined as in Eqs. (23) to (28).

$$\mathbf{G} = \begin{bmatrix} \mathbf{G}_{ao} \\ \mathbf{G}_{io} \\ \mathbf{G}_{fr} \end{bmatrix} = \begin{bmatrix} \mathbf{0} & \mathbf{0} \\ \mathbf{G}_{PMD} & \mathbf{G}_{ADR} \\ \mathbf{0} & \mathbf{0} \end{bmatrix} \tag{23}$$

$$\mathbf{G}_{PMD} = \begin{bmatrix} 0 & \cdots & \\ \vdots & \ddots & \\ \frac{N_{PMD_1}}{V_1} & \frac{N_{PMD_2}}{V_2} & \cdots \quad \frac{N_{PMD_{N_s-j}}}{V_{N_s-j}} \\ -\frac{N_{PMD_1}}{V_1} & 0 & \cdots \\ \vdots & \ddots & \end{bmatrix} \tag{24}$$

$$\mathbf{G}_{ADR} = \mathbf{G}_{thr}\mathbf{G}_{y\%} \begin{bmatrix} 0 & \cdots & \\ 0 & \ddots & \\ -\frac{N_{ADR_{max}}}{V_1} & 0 & \cdots \\ 0 & \ddots & \end{bmatrix} \tag{25}$$

$$\mathbf{G}_{thr} = \begin{bmatrix} \frac{1}{2}\left(1 + \frac{y_1 - y_{thr}}{|y_1 - y_{thr}|}\right) & 0 & \cdots \\ 0 & \ddots & \\ \vdots & & \end{bmatrix} \tag{26}$$

$$\mathbf{G}_{y\%} = \begin{bmatrix} \frac{y_1}{\Sigma_i^{N_s} y_i} & 0 & \cdots \\ 0 & \ddots & \\ \vdots & & \end{bmatrix} \tag{27}$$

$$\mathbf{C} = \begin{bmatrix} \frac{1}{V_i} \frac{N_{i_L}}{1 year} \\ \vdots \end{bmatrix} \tag{28}$$

The matrix **G** maps the control inputs to changes in the environment acting on the population of inactive objects and it is used to incorporate practical constraints and limitations in the control implementation. In particular, $\mathbf{G}_{PMD}$ in Eq. (24) defines how PMD percentages are applied across controlled shells, as detailed in Eq. (5). The number of objects at EOL in each shell is retrieved and moved from the controlled shells to the region below the 630 km compliance threshold. Eq. (25) maps the removals described in Eq. (5), 5 removals per year, and incorporates practical constraints and limitations in the control implementation. Specifically, considering the initial index distribution in Fig. 5, ADR is applied only in shells where the index exceeds the threshold of $y_{thr} = 1 \times 10^{-2}$ through Eq. (26). The available annual removals are distributed across shells in proportion to their index contribution in Fig. 5, following Eq. (27).

Finally, the **C** vector includes external disturbances and in particular the launch traffic, modeled as described in Eq. (5) through the 5-year cyclic introduction of objects in each shell.

The performance function in Eq. (12) for this application also incorporates spatially varying penalties through the weighting matrices **A** and **B**, as defined in Eqs. (29)–(36).

$$\mathbf{A} = \begin{bmatrix} \frac{1}{\Delta y_1^2 t_f} & 0 & \cdots \\ 0 & \ddots & \\ \vdots & \cdots & \frac{1}{\Delta y_{N_s}^2 t_f} \end{bmatrix} \mathbf{W}_{y\%}\mathbf{W}_{w_A} \tag{29}$$

$$\mathbf{W}_{y\%} = \begin{bmatrix} \frac{1}{1 - \frac{y_1}{\Sigma_i^{N_s} y_i}} & 0 & \cdots \\ 0 & \ddots & \end{bmatrix} \tag{30}$$

$$\mathbf{W}_{w_A} = \begin{bmatrix} 0.01_{h_1} \\ \vdots \\ 0.01_{h_{<630\ km}} \\ 1_{h_{>630\ km}} \\ \vdots \\ 1_{h_f} \end{bmatrix} \tag{31}$$

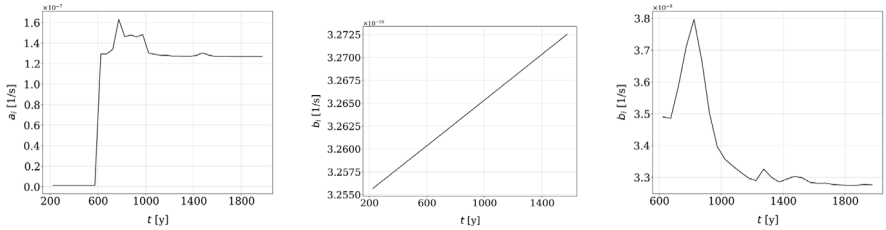

(a) Initial distribution of the **A** matrix values in Equation (12).

(b) Initial distribution of the **B** matrix part weighting PMD actions in Equation (12).

(c) Initial distribution of the **B** matrix part weighting ADR actions in Equation (12)

Fig. 6. Initial distribution of the weight matrices in Eq. (12). **A** matrix (a), **B** matrix weighting PMD control (b), **B** matrix weighting ADR control (c).

$$\mathbf{B} = \mathbf{W}_{\Delta}\mathbf{W}_{h\%}\begin{bmatrix}\mathbf{1} & \\ & \mathbf{W}_{\dot{\eta}\%}\end{bmatrix}\mathbf{W}_{w_B} \tag{32}$$

$$\mathbf{W}_{\Delta} = \begin{bmatrix} \frac{1}{\Delta u^2_{PMD_i} t_f} & 0 & \dots & \\ 0 & \ddots & & \\ \vdots & & \frac{1}{\Delta u^2_{ADR_i} t_f} & \\ & & & \ddots \end{bmatrix} \tag{33}$$

$$\mathbf{W}_{h} = \begin{bmatrix} \frac{1}{1-\frac{r_i}{\sum_{i=N_s-j}^{N_s} r}} & 0 & \dots \\ 0 & \ddots & \end{bmatrix} \tag{34}$$

$$\mathbf{W}_{\dot{\eta}\%} = \begin{bmatrix} \frac{1}{1-\frac{\dot{\eta}_1}{\sum_{i=N_s-j}^{N_s} \dot{\eta}_i}} & 0 & \dots \\ 0 & \ddots & \end{bmatrix} \tag{35}$$

$$\mathbf{W}_{w_B} = \begin{bmatrix} 1_{PMD_{N_s-j}} \\ \vdots \\ 1_{PMD_{h_{N_s}}} \\ 10_{ADR_{N_s-j}} \\ \vdots \\ 10_{ADR_{h_{N_s}}} \end{bmatrix} \tag{36}$$

The matrix **A** in Eq. (29) weights deviations from the desired target throughout the simulation time. Each shell i is weighted according to the maximum acceptable error on the output (Δy_i), multiplied by the simulation time t_f. Larger deviations result in higher penalties in the performance metric, driving the controller to reduce these gaps. Additional weight is enforced based on the local share of the total index in the environment in Eq. (30) (based on Fig. 5(c)), further prioritizing control actions in regions with higher index values and penalizing unequal distribution of the same. Finally, higher penalty is given to those shells that are above the accepted re-entry limit of objects, where the control will act (see Eq. (31)), ensuring that the controller focuses on these regions while allowing small index errors at lower altitudes to grow. The initial **A** matrix terms are given in Fig. 6(a).

The matrix **B** in Eq. (32) penalizes the control actions throughout the simulation time. Each action is weighted on the maximum allowed control effort (Δu in Eq. (33), which is set to 1 for α and β, maximum percentage of PMD or ADR), multiplied by the simulation time t_f. This means that throughout the simulation this soft constraint is used to give larger penalties to excessive control efforts. For both ADRs and PMDs greater weight is placed on actions at higher altitudes through Eq. (34), reflecting their larger cost of implementation at increasing orbital distances from Earth. Additionally, ADR control weights are influenced by the local collision rate of one intact object, namely the ADR spacecraft, with small debris, defined through $\dot{\eta}$ as in the first relation of Eq. (7) with $n_{ao_i} = 1/V_i$ in each shell i, further increasing the cost of ADR missions in more hazardous regions with Eq. (35). This bias naturally shifts the control preference towards PMD over ADR when feasible, which is further enhanced with an additional penalty on ADR in Eq. (36), as PMD actions are less complex and less resource-intensive. The initial **B** matrix distribution penalizing PMD and ADR controls is given in Figs. 6(b, c). The weights have been accurately selected to uniform the different contribution of the cost function J and enforce the penalties with relative magnitudes. Weights values in Eqs. (30), (31), (34), (35), (36) lie between 0 and 1, being relative values. Exceptions are the matrices in Eqs. (29) and (33). Based on the order of magnitude of the initial index error profile in Fig. 5, the maximum acceptable error in Eq. (29) is set to 5e-2, while the maximum acceptable control effort in Eq. (32) is set to 1, being both α and β in Eq. (5) decimals. With these choices, the integral terms at each time step in Eq. (12) remain of comparable magnitude, supporting numerical stability, while placing a slightly larger penalty on the output errors. This encourages stronger control actions to reduce deviations from the target. The greater the difference between these penalties, the more aggressively the controller is expected to close the gap with the desired output.

Finally, matrix $\mathbf{S}_f$ in Eq. (12) is set to a constant diagonal matrix weighting the final error in all the shells by $1/\Delta y^2$, with Δy equal to the value used in Eq. (29).

The resulting index profile after 100 years of simulation is shown in Fig. 7, alongside the target profile and the initial distribution. The evolutions of the index and absolute error are given in Figs. 8(a, b), while Fig. 8(c) displays the evolution of the performance function, showing a steady increase over time due to the integral nature of its formulation in Eq. (12). Fig. 9 illustrates the temporal variation of the **A** and **B** matrices diagonal terms. The **B** matrix is divided into the PMD and ADR contributions, and accordingly to the **B** definition in Eq. (32), the PMD part is not dependent on time. The controlled simulation yields a redistribution of the initial index profile, by decreasing the index in the region with the largest initial value and allowing growth elsewhere. However, the control resources are limited and highly penalized and the final profile does not fully match the desired outcome across the entire domain. At the beginning of the simulation, the control logic prioritizes reducing the performance metric contributions between 700 km and 800 km. It focuses on the region with the highest initial index, where PMD can be enforced at a reduced cost, bringing it closer to the target. As the simulation progresses, the deviation of the index value from the target between 800 km and 1000 km increases. At the same time the weights on the error in Fig. 9 impose a moderately higher penalty in this region, consistent with the beneficial redistribution prescribed by Eq. (30). Consequently, the control actions slowly shift to higher altitudes, specifically between 800 km and 1000 km. In contrast, errors in other regions, such as above 1000 km, are considered acceptable during the simulation given the prioritization of the limited

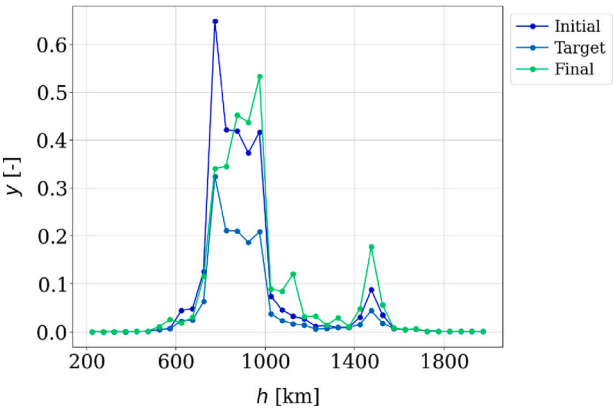

Fig. 7. Spatial index distribution at the initial simulation time and the final year. These are compared with the target profile.

control effort allocation to reduce index values in regions where it is high. Looking at Fig. 9 it is clear that PMD application would cost less than ADR and at lower altitudes, differently ADR implementation would be less expensive at higher altitude, due to the additional scaling on collision rate in Eq. (35). However, the **A** matrix weights force the controller to act on the shells below 1000 km, as long as the index value is much larger than at higher altitudes, even in expense of greater mitigation cost from ADR.

The spatial and temporal evolution of object distributions over 100 years of simulation is shown in Figs. 10, 11 and 12, along with the total number of objects in the environment at different epochs of the simulation. The dynamics of active intact objects are primarily governed by the launch traffic term (see Eq. (5)). Objects reaching EOL become inactive, and only a small proportion of active satellites are assumed to fragment due to collisions. This leads to an oscillatory pattern in the evolution of the active objects number. Following an initial adjustment period of approximately eight years, that corresponds to the payloads' lifetime relative to the launch cycle, the active object distribution settles into a cyclical pattern like the launch model. For the initial 8 years of simulation launches and disposals are not resonant, due to the non-synchronized 5-years cycle for launches and the 8-years life cycle of payloads, whose contribution is more significant than rocket bodies. Consequently, the number of intact objects grows to a peak, while in the following years, given the constant launch cycle and fixed orbital lifetimes (with no drag-induced decay), the yearly influx and passivation of objects stabilize in the affected orbital shells.

Inactive objects are directly influenced by control actions, whose distributions are in Figs. 13 and 14, while other species are only affected indirectly through collisions. Control actions are implemented above the accepted atmospheric re-entry limit of 630 km. Fig. 11 shows how launch-related cyclic behavior affects inactive object distribution, especially below 630 km, where disposed objects are placed. However, the variability in disposed objects number (linked to the control variable β) prevents complete periodicity.

Most control efforts are concentrated between 700 km and 1000 km, in line with the higher values of the index shown in Fig. 5. The initial adjustment period is also visible in Fig. 11, as PMD actions, based on launch traffic, become significant after more and more objects reach EOL (after 8 years from launch for payloads and 0.001 years for rocket bodies). Their launch-based periodicity is reflected in the evolution of inactive object numbers. The average trend shows an initial rise in inactive objects, followed by a decline, in line with increasing ADR application over time (see Fig. 14). Between 700 km and 1000 km, the control system actively reduces the number of inactive objects, while above this range, the population is allowed to grow being the index smaller and control more penalized. Fragment generation from in-orbit collisions is indirectly affected by the redistribution of intact objects. Initially, control prioritizes reducing the highest peak in the index near 750 km and the overall number of fragments decreases, thanks to combined PMD and ADR efforts targeting the inactive population near the original fragment peak. This results in a shift of the fragment peak towards higher altitudes, as illustrated in Fig. 12. The objects density remains highest between 700 km and 1000 km, due to the large number of inactive objects that continue to produce fragments through collisions. Since PMD, tied to launch traffic, is effective mainly below 750 km, early ADR demands are limited. As object densities grow above 750 km, where PMD is less effective, ADR efforts are reallocated towards higher shells, particularly just below 1000 km where the index deviation from target had grown and where PMD cannot operate efficiently, in expense of a larger control cost as shown in Fig. 9(c). The limited ADR rate forces trade-offs between competing regions. As Figs. 7, 13 and 14 show, the controller seeks an optimal distribution of mitigation efforts. The control strategy revealed by the simulation provides valuable insights into how mitigation efforts should adapt over time to environmental conditions, still limiting the performance cost. PMD is treated as the primary mechanism to achieve the target scenario, and although full saturation is not achieved, its strategic combination with ADR yields significant improvements in the redistribution and limitation of the output metric. ADR, acting where PMD is ineffective, changes in spatial application over time. After approximately 50 years, the control scheme requires ADR to operate in different orbital regions to maintain progress towards a sustainable environment. However, this shift in control allocation is bound to the penalties evolution and control effort cost.

To evaluate the effectiveness of the adaptive control approach, a comparison was made with a reference simulation employing a classical, non-controlled, but user-enforced, mitigation strategy. In this reference scenario (black lines of the Simulated case in the following figures), PMD was enforced at 99% uniformly, and 5 ADR operations per year were consistently executed in predefined orbital shells (2 ADRs at 775 km; 1 ADR each at 825, 875, and 975 km), where the index value was highest according to observations at initial time. This case scenario was chosen as comparison to simulate the decision process that brings to the definition of mitigation strategies based only on current observations of the environment. Many works in literature investigated smart ADR allocation based on a changing metric for long-term strategies (e.g. [29,52]). In the application described in the following we add the capability of taking into account cost considerations for an optimal and automatic allocation of resources. Fig. 15 shows the final index distribution obtained with the Simulated case and the Controlled case and compares the final absolute error of the two scenarios with respect to the target ($\mathbf{e} = |\mathbf{y}_f - \mathbf{y}_t|$). As expected, the Simulated scenario achieves greater reduction in the index near 750 km, reflecting its fixed ADR allocation. However, this does not necessarily result in a closer match to the target distribution. Below 1000 km, where the index increases with time, the Controlled scenario yields generally lower error than the Simulated case. Above 1000 km, the Simulated case performs better due to its uniformly maximum PMD, which is often unrealistic in practice. However, the index values above 1000 km are lower than in more critical regions. Therefore, in the Controlled case, resources are preferentially allocated to more impactful zones, reflecting real-world constraints. Overall, both scenarios achieve comparable performance, but the Controlled approach does so with a significantly reduced control effort. This is clearly illustrated in Fig. 16, which shows the respective numbers of ADR and PMD operations. The Simulated scenario utilizes the full capacity of available mitigation actions, leading to a much higher overall cost (see Fig. 17). In conclusion, the adaptive control strategy effectively balances performance and cost, dynamically allocating mitigation where it is most impactful. This demonstrates the capability of the proposed control framework to accommodate complex, real-world constraints and to

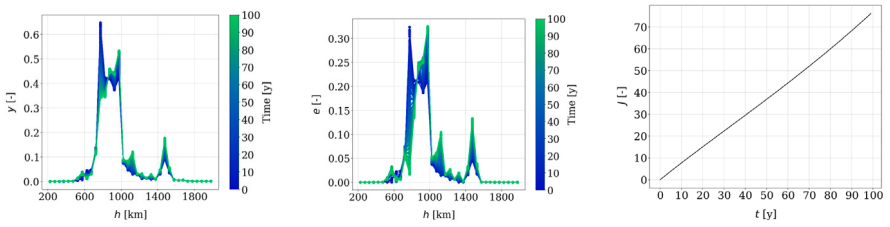

(a) Spatial and temporal 2D evolution of the index distribution.

(b) Spatial and temporal 2D evolution of the index absolute error with respect to the target.

(c) Performance function cumulative value throughout the simulation.

Fig. 8. Spatial and temporal evolution of the index (a). Spatial and temporal evolution of the error **e** in Eq. (12) (b). Performance function temporal evolution (c).

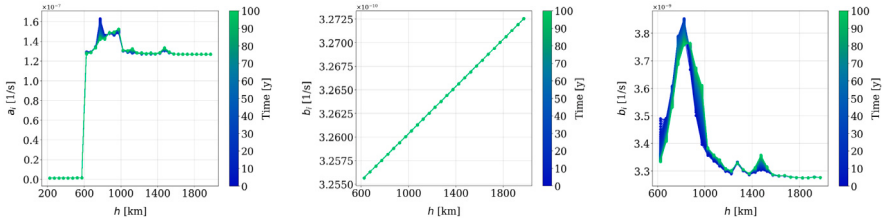

(a) Spatial and temporal 2D evolution of the **A** matrix in Equation (12).

(b) Spatial and temporal 2D evolution of the **B** matrix part weighting PMD actions in Equation (12).

(c) Spatial and temporal 2D evolution of the **B** matrix part weighting ADR actions in Equation (12)

Fig. 9. Spatial and temporal evolution of the weight matrices in Eq. (12). **A** matrix (a), **B** matrix weighting PMD control (b), **B** matrix weighting ADR control (c).

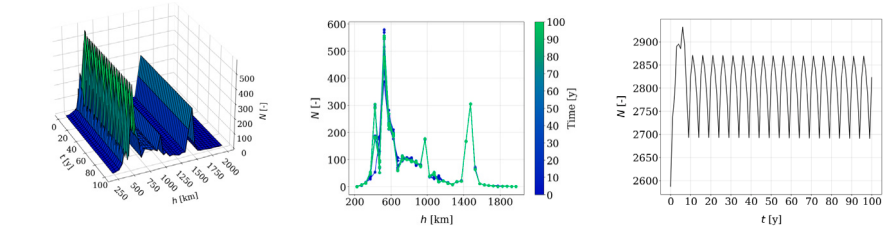

(a) 3D temporal and spatial evolution of the number of active intact objects in the shells of the domain. The colormap goes from blue to green with increasing values on the z-axis.

(b) 2D temporal and spatial evolution of the total number of active intact objects.

(c) Yearly evolution of the total number of active intact objects.

Fig. 10. Number of active intact objects distribution in the environment (a) and total number of active intact objects in the environment (b) per-year simulated.

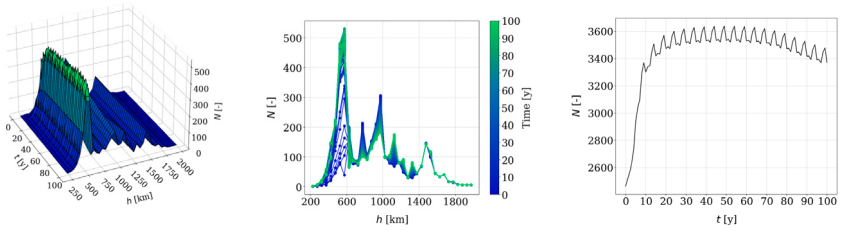

(a) 3D temporal and spatial evolution of the number of inactive intact objects in the shells of the domain. The colormap in (a) goes from blue to green with increasing values on the z-axis.

(b) 2D temporal and spatial evolution of the number of inactive intact objects in the shells of the domain.

(c) Yearly evolution of the total number of inactive intact objects.

Fig. 11. Number of inactive intact objects distribution in the environment (a) and total number of active intact objects in the environment (b) per-year simulated.

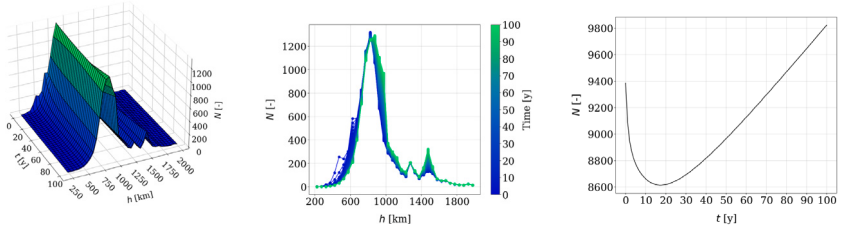

(a) 3D temporal and spatial evolution of the number of fragments in the shells of the domain. The colormap in (a) goes from blue to green with increasing values on the z-axis.

(b) 2D temporal and spatial evolution of the number of fragments in the shells of the domain.

(c) Yearly evolution of the total number of fragments.

Fig. 12. Number of fragments distribution in the environment (a) and total number of active intact objects in the environment (b) per-year simulated.

prioritize mitigation strategies based on environmental risk, resource availability, and strategic effectiveness. The strength of the approach lies in its ability to adapt control strategies over long-term horizons, responding automatically to changes in the orbital environment. These results provide valuable guidance for the development of efficient, cost-effective long-term debris mitigation plans.

5. Conclusions

The proliferation of space debris is a growing environmental threat to Earth's orbital environment, posing serious risks to the long-term sustainability of space operations. As the commercial space sector expands rapidly, existing regulatory frameworks have struggled to keep pace. This highlights the urgent need for tools that can both evaluate and inform mitigation strategies. This work introduces a foundational element of the GREEN SPECIES framework, an interdisciplinary project funded by the European Research Council, which aims to establish a controlled, socio-economic system for managing space debris. By linking environmental models with a feedback control system, the framework enables the dynamic allocation of mitigation actions to reach defined sustainability goals. A simplified, one-dimensional model simulates the evolution of three object categories: active satellites, inactive objects, and fragments; under various influences, including drag, collisions, launches, and disposal measures. A state-dependent linear feedback controller, based on the differential Riccati approach, is used to steer the system towards a target scenario while minimizing a quadratic cost function. The method accommodates soft constraints and implementation limitations, providing flexible and efficient mitigation planning. Results show the controller's effectiveness in getting closer to the target environmental metrics while balancing resource use, offering insights into optimal deployment of post-mission disposal and active debris removal. This approach provides a valuable tool for guiding space policy and supporting the development of cost-effective and adaptive sustainability strategies. Future work will explore alternative control logics, input combinations, and cost functions, along with improved definitions of sustainability targets. While the current model is deliberately low-dimensional to facilitate control integration, future developments will connect the strategy with COMETA [4], a more complex and realistic environmental model of the space population, enabling deeper validation under real-world conditions. By integrating modeling, control theory, and policy considerations, the GREEN SPECIES framework offers a novel path forward for research

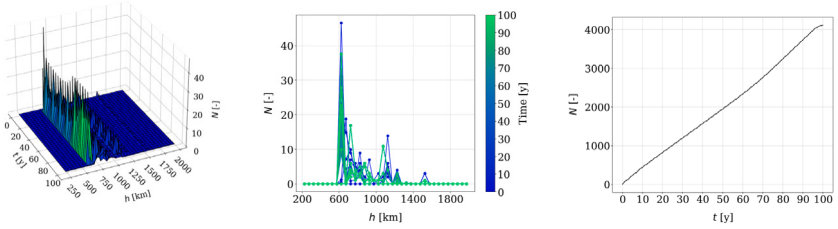

(a) 3D temporal and spatial evolution of the number of PMD performed in the shells of the domain throughout the simulation. The colormap in (a) goes from blue to green with increasing values on the z-axis.

(b) 2D temporal and spatial evolution of the number of PMD performed in the shells of the domain throughout the simulation.

(c) Yearly evolution of the cumulative total number of PMD performed.

Fig. 13. Spatial and temporal evolution of the number of PMD performed in the environment (a) and cumulative total number of PMD simulated (b).

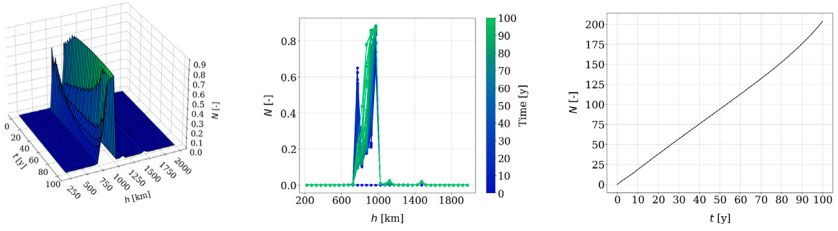

(a) 3D temporal and spatial evolution of the number of ADR performed in the shells of the domain throughout the simulation. The colormap in (a) goes from blue to green with increasing values on the z-axis.

(b) 2D temporal and spatial evolution of the number of ADR performed in the shells of the domain throughout the simulation.

(c) Yearly evolution of the cumulative total number of ADR performed.

Fig. 14. Spatial and temporal evolution of the number of ADR performed in the environment (a) and cumulative total number of ADR simulated (b).

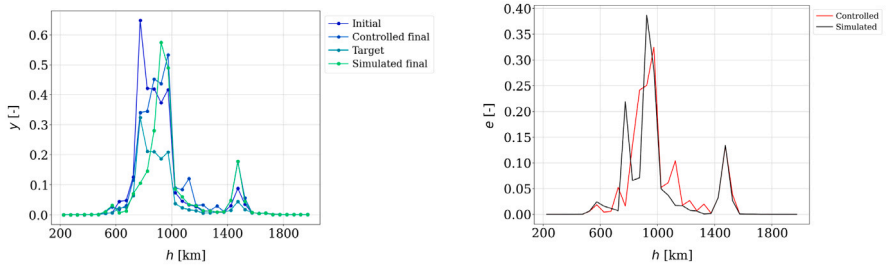

(a) Spatial index distribution at the initial simulation time and the final year for the 'Simulated' and 'Controlled' scenarios. These are compared with the target profile.

(b) Spatial distribution of the absolute error per shell between the final index value in the 'Simulated' (black) and 'Controlled' (red) cases with respect to the target one.

Fig. 15. Comparison of spatial index distribution between the 'Simulated' (black) and 'Controlled' (red) cases (a) and of their absolute error per shell with respect to the target profile (b).

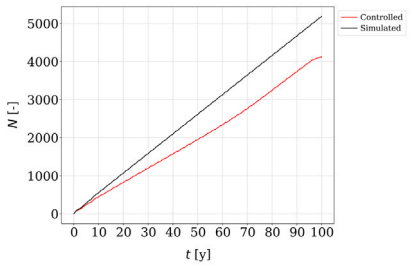

(a) Cumulative number of PMD performed during the simulations of the 'Controlled' (red) and 'Simulated' (black) cases.

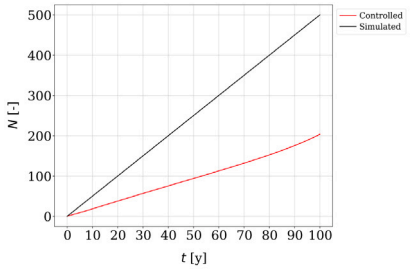

(b) Cumulative number of ADR performed during the simulations of the 'Controlled' (red) and 'Simulated' (black) cases.

Fig. 16. Comparison of the cumulative number of control effort used in the 'Simulated' (black) and 'Controlled' (red) cases.

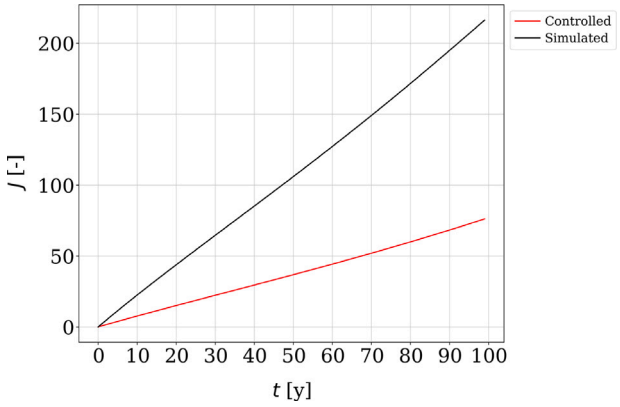

Fig. 17. Comparison of the performance function cumulative value throughout the simulation of the 'Controlled' (red) and 'Simulated' (black) cases.

and decision-making in sustainable space operations. Its versatility and extensibility suggest it may become a valuable tool not only for scientific inquiry but also for informing regulators and stakeholders about efficient, adaptive, and responsible approaches to space debris mitigation.

CRediT authorship contribution statement

Martina Rusconi: Writing – review & editing, Writing – original draft, Methodology, Investigation, Formal analysis, Data curation, Conceptualization. **Camilla Colombo:** Writing – review & editing, Supervision, Project administration, Funding acquisition.

Declaration of competing interest

The authors declare that they have no known competing financial interests or personal relationships that could have appeared to influence the work reported in this paper.

Acknowledgments

This research received funding from the European Research Council (ERC) under the European Union's Horizon Europe research and innovation program as part of the GREEN SPECIES project (Grant agreement No 101089265). The simulations have been performed using as reference population the data in [49], kindly provided by the European Space Agency.

References

[1] D. Kessler, N. Johnson, J.-C. Liou, M. Matney, The kessler syndrome: implications to future space operations, in: Advances in the Astronomical Sciences, vol. 137, 2010, pp. 47–62.
[2] D.L. Talent, Analytic model for orbital debris environmental management, Journal of Spacecraft and Rockets 29 (4) (1992) 508–513, http://dx.doi.org/10.2514/3.25493.
[3] A. Rossi, L. Anselmo, A. Cordelli, P. Farinella, C. Pardini, Modelling the evolution of the space debris population, Planetary and Space Science 46 (11) (1998) 1583–1596, http://dx.doi.org/10.1016/S0032-0633(98)00070-1.
[4] L. Giudici, C. Colombo, A. Horstmann, F. Letizia, S. Lemmens, Density-based evolutionary model of the space debris environment in low-earth orbit, Acta Astronautica 219 (2024) 115–127, http://dx.doi.org/10.1016/j.actaastro.2024.03.008.
[5] B.B. Virgili, Delta debris environment long-term analysis, in: Proceedings: 6th International Conference on Astrodynamics Tools and Techniques, ICATT, 2016.
[6] J.-C. Liou, D. Hall, P. Krisko, J. Opiela, LEGEND – a three-dimensional LEO-to-GEO debris evolutionary model, Advances in Space Research 34 (5) (2004) 981–986, http://dx.doi.org/10.1016/j.asr.2003.02.027.
[7] A. Rossi, L. Anselmo, C. Pardini, R. Jehn, G. Valsecchi, The new space debris mitigation (sdm 4.0) long term evolution code, in: Proceedings: 5th European Conference on Space Debris, 2009.
[8] H.G. Lewis, A.E. White, R. Crowther, H. Stokes, Synergy of debris mitigation and removal, Acta Astronautica (2012) 62–68, http://dx.doi.org/10.1016/j.actaastro.2012.06.012.
[9] F. Letizia, S. Lemmens, B.B. Virgili, H. Krag, Application of a debris index for global evaluation of mitigation strategies, Acta Astronautica (2019) 348–362, http://dx.doi.org/10.1016/j.actaastro.2019.05.003.
[10] IADC Steering Group and Working Group 4, IADC Space Debris Mitigation Guidelines, Tech. Rep., Inter-Agency Space Debris Coordination Committee, 2021.
[11] ESA Space Debris Office, ESA's Annual Environment Report, Tech. Rep., European Space Agency, 2024.
[12] W. Nordhaus, Chapter 16 - Integrated economic and climate modeling, in: Handbook of Computable General Equilibrium Modeling, vol. 1, Elsevier, 2013, pp. 1069–1131, http://dx.doi.org/10.1016/B978-0-444-59568-3.00016-X.
[13] P. Farinella, A. Cordelli, The proliferation of orbiting fragments: A simple mathematical model, Planetary and Space Science 2 (4) (1991) 365–378, http://dx.doi.org/10.1080/08929889108426373.
[14] D. Finkleman, Debris removal to reduce risk, in: 52nd Aerospace Sciences Meeting, 2014, http://dx.doi.org/10.2514/6.2014-0301.
[15] H. Lewis, G. Swinerd, R. Newland, A. Saunders, The fast debris evolution model, Advances in Space Research 44 (5) (2009) 568–578, http://dx.doi.org/10.1016/j.asr.2009.05.018.
[16] G.L. Somma, H. Lewis, C. Colombo, Increasing ADR effectiveness via an altitude-shell-dependent removal approach, in: Proceedings: 68th International Astronautical Congress, 2017, http://dx.doi.org/10.13140/RG.2.2.32967.55207.
[17] R.M. Tian, K. Xi, G. Lavezzi, M. Lifson, S. Servadio, R. Linares, Optimizing active debris removal strategies with feedback control for a sustainable space environment, in: Proceedings: Astrodynamics Specialist Conference, 2024.
[18] J. Zhang, Y. Yuan, K. Yang, L. Li, Long-term evolution of the space environment considering constellation launches and debris disposal, IEEE Transactions on Aerospace and Electronic Systems 59 (5) (2023) 6124–6137, http://dx.doi.org/10.1109/TAES.2023.3274097.
[19] W.B. Heard, Dispersion of ensembles of non-interacting particles, Astrophysics and Space Science (1976) p. 63–82, http://dx.doi.org/10.1007/BF00640556.

[20] C. McInnes, Simple analytic model of the long-term evolution of nanosatellite constellations, Journal of Guidance Control and Dynamics 23 (2000) http://dx.doi.org/10.2514/2.4527.
[21] N. Smirnov, A. Nazarenko, A. Kiselev, Modelling of the space debris evolution based on continua mechanics, vol. 473, European Space Agency, (Special Publication) ESA SP, 2001, pp. 391–396.
[22] N. Johnson, P. Krisko, J.-C. Liou, P. Anz-Meador, NASA's new breakup model of evolve 4.0, Advances in Space Research 28 (9) (2001) 1377–1384, http://dx.doi.org/10.1016/S0273-1177(01)00423-9.
[23] F. Letizia, C. Colombo, H.G. Lewis, Analytical model for the propagation of small-debris-object clouds after fragmentations, Journal of Guidance Control and Dynamics 38 (8) (2015) 1478–1491, http://dx.doi.org/10.2514/1.G000695.
[24] S. Frey, C. Colombo, S. Lemmens, Application of density-based propagation to fragment clouds using the starling suite, in: Proceedings: First International Orbital Debris Conference, 2019.
[25] L. Giudici, C. Colombo, A. Horstmann, F. Letizia, S. Lemmens, Density-based evolutionary model of the space debris environment in low-earth orbit, Acta Astronautica (2024) http://dx.doi.org/10.1016/j.actaastro.2024.03.008.
[26] C. Colombo, F. Letizia, H. Lewis, Spatial density approach for modelling of the space debris population, in: Proceedings: AAS/AIAA Space Flight Mechanics Meeting, 2016.
[27] C. Duran, L. Giudici, C. Colombo, Modelling the whole space debris environment through a spatial density approach, in: Proceedings: AAS/AIAA Astrodynamics Specialist Conference, 2021.
[28] J.C.V. Escobar, Continuum Approach for the Modelling of Debris Population and Launch Traffic in Low Earth Orbit (Ph.D. thesis), Politecnico di Milano, 2022, URL https://hdl.handle.net/10589/187251.
[29] A.E. White, H.G. Lewis, An adaptive strategy for active debris removal, Advances in Space Research 53 (8) (2014) 1195–1206, http://dx.doi.org/10.1016/j.asr.2014.01.021.
[30] D.J. Kessler, Derivation of the collision probability between orbiting objects: the lifetimes of jupiter's outer moons, Icarus 48 (1) (1981) 39–48, http://dx.doi.org/10.1016/0019-1035(81)90151-2.
[31] R.J. LeVeque, Finite volume methods for hyperbolic problems, in: Cambridge Texts in Applied Mathematics, Cambridge University Press, 2002.
[32] F. Letizia, Extension of the density approach for debris cloud propagation, Journal of Guidance Control and Dynamics 41 (12) (2018) 2651–2657, http://dx.doi.org/10.2514/1.G003675.
[33] L. Giudici, C. Colombo, Space debris density propagation through a finite volume method, in: 33rd AAS/AIAA Space Flight Mechanics Meeting, 2023.
[34] R.J. LeVeque, Finite volume methods for hyperbolic problems, in: Cambridge Texts in Applied Mathematics, Cambridge University Press, 2002, http://dx.doi.org/10.1017/CBO9780511791253.
[35] T. Flohrer, S. Lemmens, B.B. Virgili, H. Krag, H. Klinkrad, E. Parrilla, N. Sanchez, J. Oliveira, F. Pina, DISCOS – current status and future developments, in: Proceedings: 6th European Conference on Space Debris, 2013.
[36] F. Letizia, S. Lemmens, H. Krag, Environment capacity as an early mission design driver, Acta Astronautica 173 (2020) 320–332, http://dx.doi.org/10.1016/j.actaastro.2020.04.041.
[37] D.G. King-Hele, Theory of Satellite Orbits in an Atmosphere, (645) Butterworths Mathematical Texts, 1964, http://dx.doi.org/10.1002/qj.49709038627.
[38] S. Frey, C. Colombo, S. Lemmens, Extension of the King-Hele orbit contraction method for accurate, semi-analytical propagation of non-circular orbits, Advances in Space Research 64 (1) (2019) 1–17, http://dx.doi.org/10.1016/j.asr.2019.03.016.
[39] F. Letizia, B.B. Virgili, S.L. S., Assessment of orbital capacity thresholds through long-term simulations of the debris environment, Advances in Space Research 72 (7) (2023) 2552–2569, http://dx.doi.org/10.1016/j.asr.2022.06.010.
[40] S.R. Nekoo, Tutorial and review on the state-dependent Riccati Equation, Journal of Applied Nonlinear Dynamics 8 (2019) 109–166, http://dx.doi.org/10.5890/JAND.2019.06.001.
[41] S. Beeler, D. Cox, State-Dependent Riccati Equation Regulation of Systems with State and Control Nonlinearities, NASA Technical Reports Server, Tech. Rep., 2004.
[42] M.H. Korayem, S.R. Nekoo, Finite-time state-dependent Riccati equation for time-varying nonaffine systems: Rigid and flexible joint manipulator control, ISA Transactions 54 (2015) 125–144, http://dx.doi.org/10.1016/j.isatra.2014.06.006.
[43] F. Topputo, M. Miani, F. Bernelli-Zazzera, Optimal selection of the coefficient matrix in state-dependent control methods, Journal of Guidance Control and Dynamics 38 (5) (2015) 861–873, http://dx.doi.org/10.2514/1.G000136.
[44] A.E. Bryson, Y.-C. Ho, G.M. Siouris, Applied optimal control: Optimization, estimation, and control, IEEE Transactions on Systems, Man, and Cybernetics 9 (6) (1979) 366–367, http://dx.doi.org/10.1109/TSMC.1979.4310229.
[45] M. Rusconi, L. Giudici, C. Colombo, Application of active feedback control for investigation of debris mitigation strategies on a density-based model of the population evolution, in: Proceedings: 75th International Astronautical Congress, IAC, 2024, http://dx.doi.org/10.52202/078360-0184.
[46] M.H. Korayem, S.R. Nekoo, State-dependent differential Riccati equation to track control of time-varying systems with state and control nonlinearities, ISA Transactions 57 (2015) 117–135, http://dx.doi.org/10.1016/j.isatra.2015.02.008.
[47] A.A. Kabanov, Finite-time state-dependent coefficient method for optimal control of nonlinear systems, in: Proceedings: International Conference on Industrial Engineering, Applications and Manufacturing, ICIEAM, 2022, pp. 717–721, http://dx.doi.org/10.1109/ICIEAM54945.2022.9787138.
[48] A. Laub, A Schur method for solving algebraic Riccati equations, IEEE Transactions on Automatic Control 24 (6) (1979) 913–921, http://dx.doi.org/10.1109/TAC.1979.1102178.
[49] F. Letizia, B.B. Virgili, S. Lemmens, Assessment of orbital capacity thresholds through long-term simulations of the debris environment, Advances in Space Research 72 (7) (2023) 2552–2569, http://dx.doi.org/10.1016/j.asr.2022.06.010.
[50] A. Rossi, G. Valsecchi, E. Alessi, The criticality of spacecraft index, Advances in Space Research 56 (3) (2015) 449–460, http://dx.doi.org/10.1016/j.asr.2015.02.027.
[51] C. Colombo, A. Muciaccia, L. Giudici, J.L. Gonzalo, A. Masat, M. Trisolini, B. Campo, F. Letizia, S. Lemmens, Tracking the health of the space debris environment with THEMIS, in: Joint 10th EUCASS - 9th CEAS Conference, 2023.
[52] L. Giudici, C. Colombo, F. Letizia, Optimal active debris removal sequence identification through combined debris index analysis and long-term projection of the orbital environment, in: 75th International Astronautical Congress, 2024, http://dx.doi.org/10.52202/078360-0166.